Iranian Journal of Hydrogen & Fuel Cell 1(2019) 23-37

Iranian Journal of Hydrogen & Fuel Cell

IJHFC

Journal homepage://ijhfc.irost.ir

Generalization of a CFD model to predict the net power in PEM fuel cells

A. Ghanbarian[1], M.J. Kermani[1,2,*], J. Scholta[3]

[1] Amirkabir Uni. of Tech., 424 Hafez Ave., 15875-4413 Tehran, Iran
[2] Adjunct Fellow, Centre for Solar Energy and Hydrogen Research (ZSW) 89081 Ulm, Germany
[3] Center for Solar Energy and Hydrogen Research (ZSW), Helmholtz str. 8, 89081 Ulm, Germany

Article Information

Article History:

Received:
29 Sep 2018
Received in revised form:
11 Apr 2019
Accepted:
23 Apr 2019

Keywords

Fuel Cells
Flow Field Design
Performance Prediction
CFD

Abstract

Qualitatively, it is already known that reactants content within the catalyst layer (CL) is the driving moments for the kinetics of reaction within the CL. The present paper is aimed to quantitatively express the level of enhancement in electrical power due to enrichment in the oxygen content. For a given MEA, a flow field (FF) designer is always willing to design a FF to maximize the content of oxygen in all regions of the CL. Using the guidelines provided in this paper, FF-designers, without a cumbrous CFD computations, can predict how much enhancement in electrical power can be achieved due to 1% enrichment in oxygen content within the CL. To answer to this question, a three dimensional CFD tool has been used. It simulates steady, single-phase flow of reactant-product of moist air mixture in the air side electrode of proton exchange membrane fuel cell (PEMFC). The task is performed for different channel geometries, all of them as parallel straight flow fields (FF), via which a relation between the oxygen content at the face of CL and the cell net power is developed. It is observed that at V=0.35 V, for 1% enrichment in oxygen content within the CL, the net power can enhance by 3.5%.

1. Introduction

Fuel cells are considered as the power sources for the future, and proton exchange membrane fuel cell (PEMFC) is one of the most important clean power generators for portable, mobile and stationary applications. PEMFCs produce zero to low emission, can operate at low temperatures, provide high power

*Corresponding Author's Fax: +49711 78 70
E-mail address: mkermani@aut.ac.ir

doi: 10.22104/ijhfc.2019.3176.1179

density and enjoy fast start up [1-5].

To achieve better operation and performance for fuel cells, enhanced design and optimization of them is necessary [6-9]. The flow field design in the bipolar plates is one of the key parameters for the efficient utilization of catalyst layers (CLs).

The PEMFC's channels act as the reactant suppliers and product collectors. The reactants, as well as the products, are transported to and from the cell through the flow channels. An appropriate flow field design can enhance the reactant delivery and product removal from the cell. This will minimize the concentration losses occurring usually at high current densities [1,3]. The bipolar plate is one of the most imperative components of fuel cells, which can occupy up to 80% of the weight and near about 50% of the total cost of the cell [13].

Maximizing the content of reacting species in all regions of catalyst layers (CL) is always the desired goal of flow field (FF) designers of fuel cells. In fact, a FF-designer in fuel cell is responsible to design a FF with better utilization of catalyst layer (CL) [11-13].

Tehlar et al. [14] developed a model to examine different channel-rib geometries and GDL characteristics. The results show that cross convection can significantly increase the current density and consequently the power density of the cell. A strong sensitivity to GDL compression, flow velocity and rib width was found. As an optimized value the GDL thickness under the rib was increased resulting in about 20% higher current densities. Precise knowledge of the GDL characteristics are key to understand channel-to-channel cross convection and optimize performance [14].

Wang et al. [15] developed a generalized model for flow field designs of the most common layout configurations with U-type arrangement, including single serpentine, multiple serpentine, straight parallel, and interdigitated configurations. The flow distribution and the pressure drop in the multiple serpentine were between the straight parallel and the single serpentine. This provides a practical guideline to evaluate how far a fuel cell is from optimized design operating conditions, and measures how to improve flow distribution and pressure drop [15].

Liu et al. [16] designed tapered channels for the cathode side of the PEMFC flow fields. By reducing the channel cross section area, the oxygen transport to the gas diffusion layer would be easier while the content of oxygen is reduced due to cathode reaction, hence, the cell performance would be increased. The results also reveal that the liquid water effect in general influences the cell performance and the effect becomes significant at lower voltages [16].

Ramesh et al. [17] studied various sizes of channel and rib width for a parallel flow field of a PEMFC to ensure uniform distribution of the fuel and oxygen to the reaction sites. The range of channel width is between 0.5 to 2 mm, and the range of rib size is 0.2 to 1.2 mm. The results reveal that the cell performance is reduced due to rib size increment but increasing in channel width cause the cell performance enhancement [17].

By a basic classification of the CFD solvers of fuel cells, two different approaches can be sought to evaluate the cell performance:

1. Approach 1: Constant sink/sources distribution within the catalyst layers. In this CFD approach, the governing equations of fluid motion are solved and, say, in cathode electrode oxygen mole fraction $(YO_2)_{CL}$ at CL/GDL interface are evaluated as part of the solution. Generally, the higher the value of $(YO_2)_{CL}$ is, the cell performance is better. However, as in this approach, no current-to-voltage relationship is used, the cell current density, voltage and power density are not evaluated. Hence, the cell performance (e.g. cell power density) can only qualitatively be said that the higher $(YO_2)_{CL}$ corresponds to higher cell power density.

2.Approach 2: Variable distribution of sink/source within the catalyst layer. In this CFD approach, in addition to the governing equations of fluid motion, a (set of) cell current-to-voltage relation is also solved. Hence, in addition to $(YO_2)_{CL}$, the cell current density and power density can be calculated for an specified cell voltage, for example. This approach (Approach 2), will allow development of a quantitative

relationship between the enhancement of cell power density due to a unit percent increase in $(YO_2)_{CL}$. This is as opposed to Approach 1 that could only provide qualitative results.

The present paper is aimed to quantitatively express the level of enhancement in electrical power (or power density) due to enrichment in oxygen content, or say oxygen mole fraction at the face of CL. A pressure based Computational Fluid Dynamics (CFD) tool has been used in the present study. The commercial software package of ANSYS® FLUENT® has been used for this purpose. The present study is performed for a given MEA, fixed operating conditions of a cell, and straight-parallel flow fields. The approach is extendable to other cases.

In this paper, 9 different channel geometries, named G_1 to G_9 are studied (see Figs. 1 and 2). The cell active area for all of the cases was taken identical. The variation of oxygen mole fraction at gas diffusion layer (GDL) and catalyst layer (CL) interface is observed, $(YO_2)_{CL}$. Investigating the numerical data, a relation between YO_2 and net power density is developed. For the cases studied, the present model provides a basic rule to predict the generated electrical power (Pg) and the net power (Pnet) by solely having knowledge of the oxygen mole fraction at the face of catalyst layer.

2.Cell net power density and oxygen mole fraction relation

For a cell with fixed MEA and operating conditions, YO_2 can be enhanced using several different variations in flow field (FF). For example, increasing channel width to rib (w/d) ratio; reducing channel height (h); increasing mass flows through the channels ($\dot{m}$); techniques that enhance over-rib-convections; etc. In all of the exampled cases the pumping power is changed; and a net power should be considered instead of the sole power generated by the cell, i.e.:

$$P_{net} = \underbrace{i.V_{cell}}_{TermI=P_g} - \underbrace{\Delta P.\dot{V}/A}_{TermII=PumpingPower} \quad (1)$$

Term I in equation. (1) represents the generated power; and Term II is the pumping power, in which ΔP is the pressure drop along the flow channel, is the average volume flow rate and A is the cell active area. The balance between Terms I and II provides the net power produced by the cell, Pnet.

Pg is the generated cell power density, determined from the cell current density i and cell voltage Vcell. In [18] it is shown that "at a fixed utilization, say 50%; for 1% enrichment in YO_2 within the CL, 0.3 to 0.4% enhancements in power density can be expected". The present paper provides a basic rule to predict Pg and Pnet by solely computing the oxygen mole fraction at the face of catalyst layer. This relation is derived using numerical data and analytical approximation. The relation will be discussed at the end of result section.

3.Problem Definition

The present paper is aimed to quantitatively determine the level of enhancement in net power due to enrichment in oxygen content within the CL. The computational domain consists of a single channel of length L, connected at the top to a Gas Diffusion Layer (GDL) over which the Catalyst Layer (CL) is placed. Fig. 1 shows the schematics of the domain. To determine the relation between the net cell power densities to oxygen mole fraction, numerical simulation of different geometries of gas channels in a fixed MEA (fixed cell active area) is done. Nine geometry cases named G_1 to G_9 that is showed in fig. 2 are numerically studied in this paper. Generally speaking, the geometrical parameters of a flow field can be defined using channel width, height and length, respectively w, h, L, and the ribs between two adjacent channels d. Based on an earlier study [19], it is found that the following ranges for the parameters channel widths, ribs, channel width over channel depth, and channel width over rib width are considered suitable.

- Channel width (w), $0.4 \leq w \leq 1.0$ mm
- Rib width (d), $d \geq 0.6$ mm

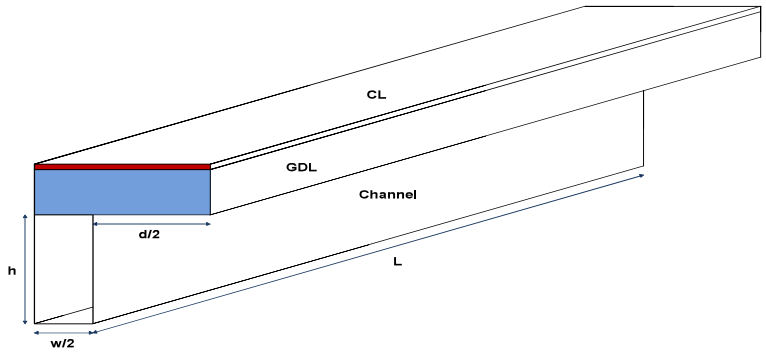

Fig. 1. Schematic of the computational domain

	Geometry G_1	Geometry G_2	Geometry G_3
Schematic picture	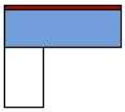	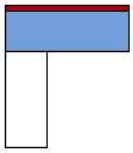	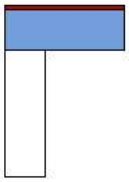
Dimension	w/2=0.25 mm d/2= 0.50 mm h=0.40 mm	w/2=0.25 mm d/2= 0.50 mm h=0.60 mm	w/2=0.25 mm d/2= 0.50 mm h=0.80 mm
	Geometry G_4	Geometry G_5	Geometry G_6
Schematic picture	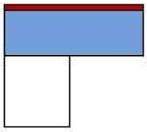	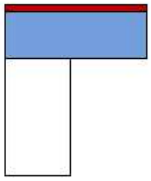	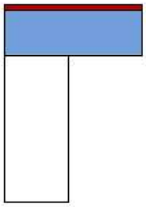
Dimension	w/2=0.35 mm d/2= 0.40 mm h=0.40 mm	w/2=0.35 mm d/2= 0.40 mm h=0.60 mm	w/2=0.35 mm d/2= 0.40 mm h=0.80 mm
	Geometry G_7	Geometry G_8	Geometry G_9
Schematic picture	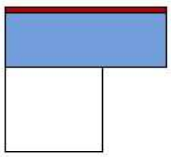	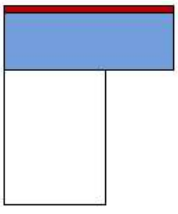	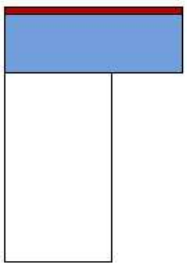
Dimension	w/2=0.45 mm d/2= 0.30 mm h=0.40 mm	w/2=0.45 mm d/2= 0.30 mm h=0.60 mm	w/2=0.45 mm d/2= 0.30 mm h=0.80 mm

Fig. 2. Frontal view of channel/GDL/CL assembly, in all the cases L= 80 mm, t_{GDL}= 0.25 mm, t_{CL}=0.025 mm

• Channel width over channel depth (w/h), w/h > 0.7
• Channel width over rib width (w/d), w/d > 0.4

The numerical values for the parameters correspond to G_1 to G_9 are shown in fig. 2.

A grid independency check was performed. Suitable grid sizes, which have been used in the present study, are reported in Table 1. This table represents the dimensions of G_1 as a sample and the number of the meshes used in the present study. All the simulations are done corresponding to a fixed MEA (fixed active area). The size of a repeating unit (channel width w plus rib width d) is constant and is equal to 1.5 mm.

The governing equations (described in section 4) are solved using an academic version of software package ANSYS® FLUENT®. To relate the voltage-to-current (v-to-c) the Tafel equation, described in section 4, is incorporated as User-Defined-Function (UDF) within the software environment. The values for other parameters are provided in Table 2.

The physical properties and operating conditions being used in the present computations are provided in Table 2.

3.1. Model Assumption

• Due to the importance of the cathode, as the performance limiting component in PEM Fuel Cells, only the cathode side is considered here.
• The flow operates under steady state conditions.
• The working fluid is a gas mixture consisting of the species oxygen, nitrogen and water, which are considered as ideal gas.
• The flow is assumed to be single phase.
• The mixture flow is assumed to be incompressible.
• The flow is considered to be laminar.
• Gravitational effects are ignored, and the flow is driven solely due to pressure gradient.
• Gas diffusion layer and catalyst layer are treated as isotropic macro-homogenous porous materials.

Table 1. Dimensions and meshes of computational domain for a sample case, G-1.

zone	Length (mm)/mesh	Width (mm)/mesh	Height (mm)/mesh	Rib width (mm)/mesh
Flow channel	80/300	0.5/10	0.4/10	1/20
Gas diffusion layer	80/300	1.5/30	0.25/7	---
Catalyst layer	80/300	1.5/30	0.025/4	---

Table 2. Physical properties and operating conditions used in the present computation

Open circuit voltage (VO.C.)	1.1 V
Cell voltage (Vcell)	0.2, 0.35, 0.5, 0.65 V
Operating temperature (T)	333K
Operating pressure (P)	101325 Pa
Faraday constant (F)	96487 C /mol
Gas constant (R)	8.314 J/mol.K
Dew point temperature ($T_{dew\ point}$)	313 K
Utilization (u)	50%
Porosity of gas diffusion layer, ε_{GDL}	0.7
Fluid viscous resistance of gas diffusion layer(1/K)	5.68×10^{10} 1/m^2
Porosity of catalyst layer, ε_{CL}	0.7
Fluid viscous resistance of gas diffusion layer(1/K)	5.68×10^{10} 1/m^2
Area specific resistance (σ)	$1\times10^{-5}\Omega$cm^2
Charge transfer coefficient (α_C)	0.5
C^{ref}_{O2}	0.233
Exchange current density (i_0)	2×10^{-5}A/cm^2

4. Governing equations

The governing equations for the channel (as a clear region) and the gas diffusion layer and catalyst layer are written in a unified form as follows, where the equations contain porosity (Ɛ) and permeability values (K). In channel region Ɛ is set to 1, and K→∞ and in GDL and CL regions, the specified values in table 2 are used for Ɛ and K. The conservation of mass for the three-species gas mixture is:

$$\frac{\partial(\varepsilon\rho)}{\partial t}+\nabla.\left(\varepsilon\rho\vec{V}\right)=S_m \tag{2}$$

where, Ɛ is porosity, ρ is density, t is time, $\overline{v}$ is velocity vector and S_m is the source term of the mixture defined later in this section. The mixture momentum equation within the channel region is:

$$\frac{\partial\left(\rho\vec{V}\right)}{\partial t}+\nabla.\left(\rho\vec{V}\vec{V}\right)=-\nabla P+\nabla.\left(\mu\nabla\vec{V}\right) \tag{3}$$

In equation 3, P is pressure and μ is fluid viscosity, the momentum equation in porous zones of GDL and CL is defined using the Darcy's law (equation 4) as:

$$\varepsilon\vec{V}=-\frac{k}{\mu}\nabla P \tag{4}$$

The mixture energy equation is:

$$\frac{\partial\left(\varepsilon\rho C_P T\right)}{\partial t}+\nabla.\left(\varepsilon\rho c_P\vec{V}T\right)=\nabla.\left(k^{eff}\nabla T\right) \tag{5}$$

Where, T is operating temperature, C_P is specific heat coefficient in constant pressure and K^{eff} is effective heat transfer coefficient. The species transport equations are written using the Fick's law as:

$$\frac{\partial\left(\varepsilon C_i\right)}{\partial t}+\nabla.\left(\varepsilon\vec{V}C_i\right)=\nabla.\left(D_i^{eff}\nabla C_i\right)+S_i \tag{6}$$

Here S_i is the species source term, where the subscript i represents O_2 and H_2O. Within the channel and GDL S_i=0. S_i within the CL will be defined in this section. To relate the voltage-to-current (v-to-c), the User Defined Function (UDF) capability of the ANSYS® FLUENT® package is used to incorporate the kinetics of reaction within the catalyst layer via the Tafel equation in the present study. This approach is able to provide the distributions for local current density i and sink/source terms S within the CL. S and i are related to each other via the Faraday law as follows. For a given cell current density i (A/m^2), the molar consumption rate of oxygen $\dot{n}_{O_2}$ is obtained from:

$$\dot{n}_{O_2}=\frac{i.A}{4F} \tag{7}$$

where A is the cell active area, and F is Faraday constant. Correspondingly, the consumed oxygen mass flow rate $\dot{m}_{O_2}$ is determined from:

$$\dot{m}_{O_2}=-M_{O_2}\dot{n}_{O_2}=-M_{O_2}\frac{i.A}{4F} \tag{8}$$

Where M_{O2} is the molecular weight of oxygen. The negative sign in equation (8) represents oxygen consumption. Hence, the oxygen S-term is obtained from:

$$S_{O_2}=\frac{\dot{m}_{O_2}}{(vol.)_{CL}} \tag{9}$$

where (vol.)CL is CL volume. Hence:

$$S_{O_2}=\frac{-M_{O_2}i}{4F}\frac{A}{(vol.)_{CL}} \tag{10}$$

Similarly, water vapor is generated with the molar rate of $\dot{n}_{H_2O}$:

$$\dot{n}_{H_2O}=\frac{i.A}{2F} \tag{11}$$

and

$$S_{H_2O}=\frac{M_{H_2O}}{2F}\frac{A}{(vol.)_{CL}} \tag{12}$$

and

$$S_m=S_{H_2O}+S_{O_2} \tag{13}$$

The current to voltage relationship is established using the Tafel equation (14), being employed within the UDF code:

(a) (b)

Fig. 3. Sample of grid configuration for: a) front view of G-1 and b) side view of G-1

$$\eta = \frac{RT}{\alpha_C F} \ln\left[\frac{iC_{O_2}^{ref}}{i_0 C_{O_2}}\right] \quad (14)$$

here i_0 is the exchange current density, C^{ref}_{O2} is the reference oxygen mass transfer, and α_C is the cathode side charge transfer coefficient. The cell voltage can, therefore, be obtained from:

$$V_{Cell} = V_{ref} - \eta - \sigma i \quad (15)$$

where σ is the overall area specific resistance of the cell, including the protonic resistance of the membrane and electronic resistances of the GDL and other parts of the cell.

Fig. 3 shows samples of the grid configurations used in the present study. To check for the solution dependency to the grid sizes, a grid independency check was performed. Suitable grid sizes, which have been used in the present study, are reported in Table 1.

5. Results and discussion

Fig. 4 shows validation in this study. It shows comparison between the polarization curve for the present computation, and the experimental data obtained from [20]. As illustrated in Fig. 4, there is an acceptable agreement between the data. Since the parameters of the validating case is different from those used in the present study (Table 2), the physical properties in the present computation are tuned to those in [19] for validation purposes, i.e. T=353 K, P=101325 Pa, inlet velocity=0.415 m/s, relative humidity at inlet =10%, and the single-phase mixture is considered to be oxygen and water vapor $\sigma = 3.65\times10^{-5}\,\Omega.m^2, \alpha_C = 0.8, i_0 = 1.5\times10^{-5}\ A/cm^2$, $\varepsilon = 0.4$, $K = 1.76\times10^{-11}\,m^2$

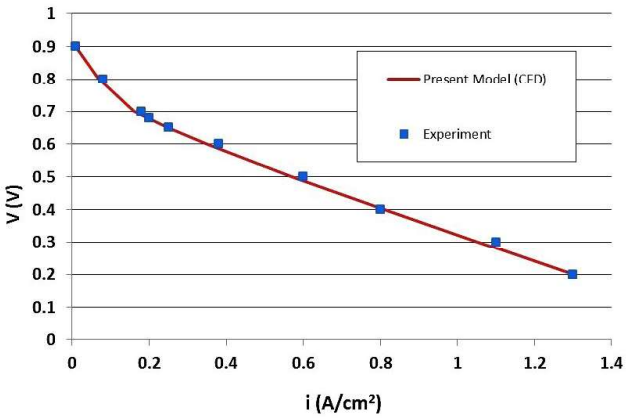

Fig 4. Validations: comparison between polarization curve for the present computation (CFD) and experimental data [20]

Computations of a straight channel flow field of a PEM fuel cell is studied in this paper. The main purpose of these studies is to derive a relation between net cell power density (Pnet) and the average of oxygen mole fraction (YO_2) at the face of reaction site in the cathode (GDL/CL interface). To estimate the main relation, channels with different cross section dimensions are analyzed (see Fig. 2).

Fig. 5 shows sample of computed results for geometry cases 1 to 9 (G_1 to G_9). The red line graphs depict the polarization curve. As expected, the current density increases by decreasing the cell voltage. Comparison of the polarization curves for cases G_1 to G_9 is discussed in fig. 6. The green line graphs

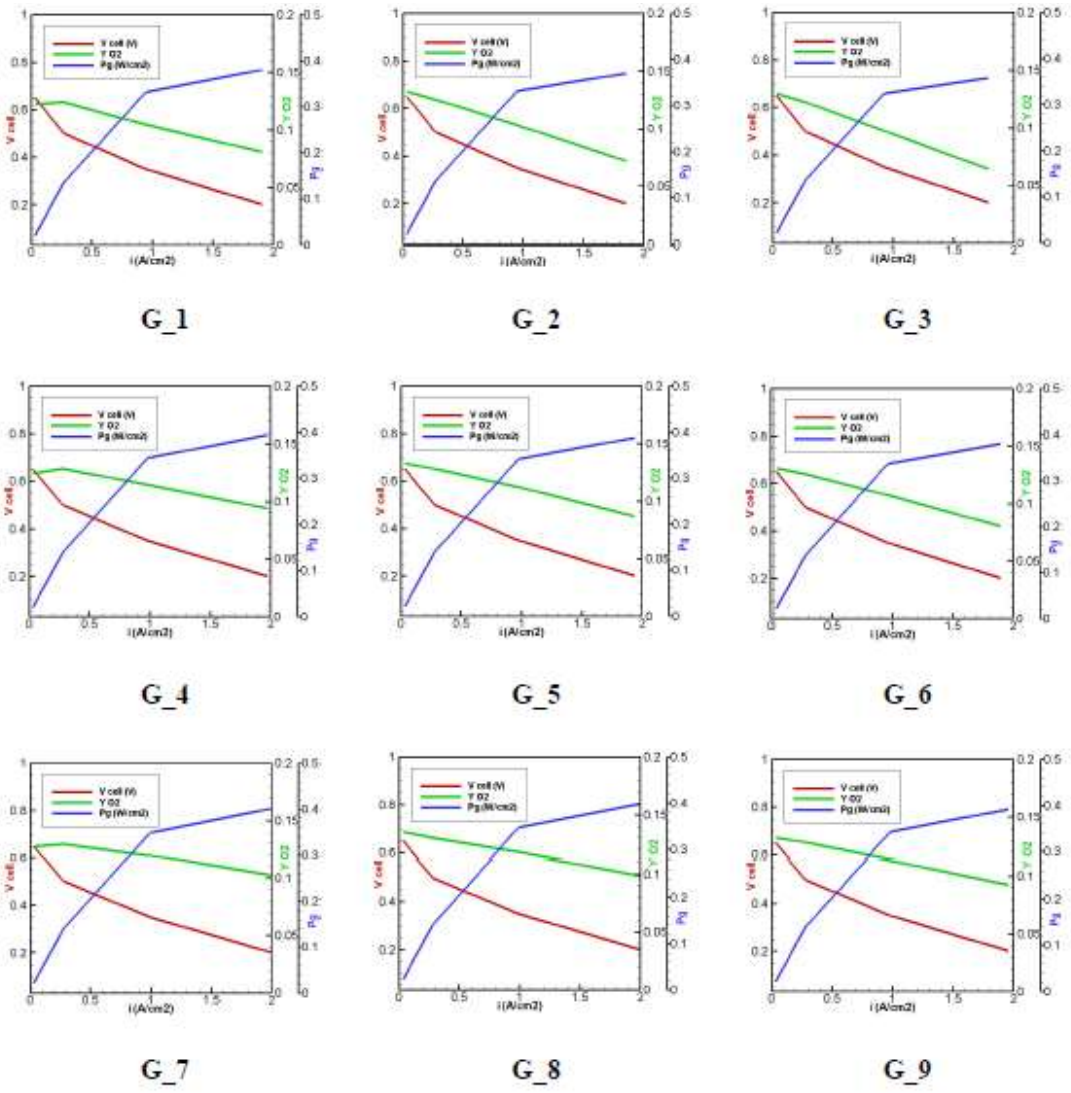

Fig. 5. Sample of computed results for constant oxygen utilization; Cell voltage, generated power density with cell current density

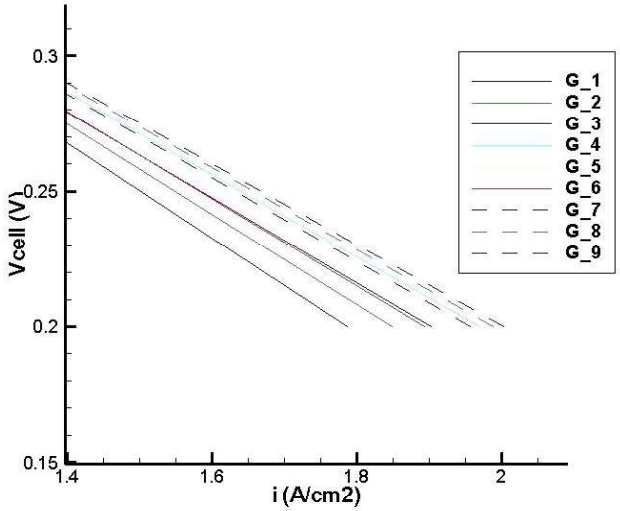

Fig. 6. Comparison of the polarization curves for cases G_1 to G_9 and constant oxygen utilization, low concentration region

show the variation of oxygen mole fraction with cell current density. In comparison with the polarization curve, this graph represents the oxygen consumption in the cathode side of the PEM fuel cell. The blue line graphs show the generated electrical power density variation with cell current density. The graph is approximately linear up to i= 1 A/cm^2. It is noted that, the numerical computations are performed at cell voltage 0.2 to 0.65 V, hence, the graphs represent the computed range, as a part of whole operating cell voltage (i.e. 0 to 1.1 V).

Fig. 6 shows comparison of the polarization curves for cases G_1 to G_9. As illustrated in this figure the most difference between the polarization curves occur in low oxygen concentration regions (high current density or low cell voltage), where the concentration losses play the main role. Fig. 7 schematically shows the share of each of the main components of the losses in a fuel cell, namely, the activation-, ohmic- and concentration-losses. Changing the gas flow channel geometry leads changing in mass transport mechanisms. Hence, concentration losses are reduced in channels with proper geometry. On the other hand, at increased cell voltages (or reduced current densities), the influence of concentration losses is low. So, changing in channel geometry performs ineffectively in low current density regions. This could be explained using a different terminology as follows. In low current density regions, the oxygen consumption rate is low. Hence, oxygen would have enough time to reach the reaction sites within the CL. On the contrary, in high current density regions, the oxygen consumption rate is high. So the reaction sites may starve for oxygen. To lessen this effect, better oxygen delivery to the reaction sites could be achieved using proper channel geometry.

Fig. 8 shows contours of oxygen mole fraction at GDL/CL interface for all cases (G_1 to G_9) for constant oxygen utilization and V= 0.35 V. As shown in this figure, the oxygen content above the channel is more than above the rib. The channel width in G_1 to G_3 is 0.5 mm, G_4 to G_6 is 0.7 mm and G_7 to G_9 is 0.9 mm for a constant active area. Fig. 8 shows that channels with

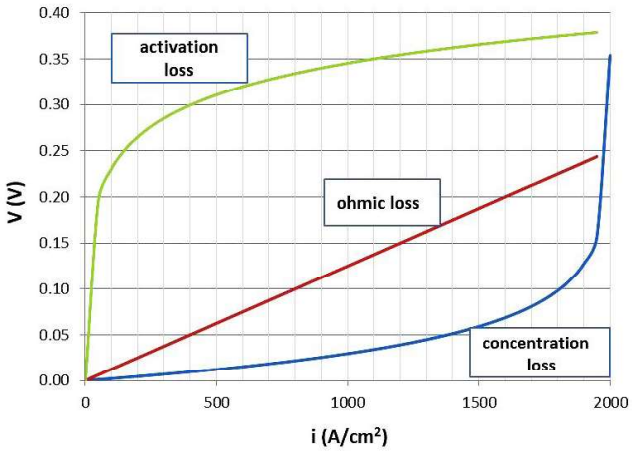

Fig. 7. Schematic contributions of the loss components from activation-, ohmic- and concentration-losses

larger channel width have more oxygen content at the face of catalyst layer (GDL/CL interface). Fig. 9 shows contours of current density at GDL/CL interface for all cases (G_1 to G_9) for constant oxygen utilization and V= 0.35 V. Comparing Figs. 8 and 9, it can be seen that YO_2 is directly proportional to the produced i. It can also be seen from Figs. 8 and 9 that, cases with larger channel width have richer oxygen contents within the CL, hence, they produce more electrical current. The results shown in Figs. 8 and 9 have been obtained based on the physical properties and operating conditions provided in Table 2 at utilization 50% and cell voltage 0.35V. Tables 3 summarizes computed results for the all the cases (G_1 to G_9) at Vcell values 0.2, 0.35, 0.5 and 0.65 V. This table refers to constant oxygen utilization 50% and contains 14 parameters. The definition for each of the parameters is provided in the footnote of Tables 3. It is noted that Table 3 reports computed results at constant utilization 50%. The mass flow and the cell current density in this table are adjusted in a trial and error procedure to ensure utilization 50%. As reported in Table 3, i increases with $Y_{O2@GDL/CL}$. The reason is explained as follows. $Y_{O2@GDL/CL}$ is the driving moment for the kinetics of reaction within the CL. The larger the $Y_{O2@GDL/CL}$ is, the quicker the kinetics of reaction within the CL will be. As indicated in Table 3, for the cases with larger mass flow and lower channel cross section area are much larger than the others. It

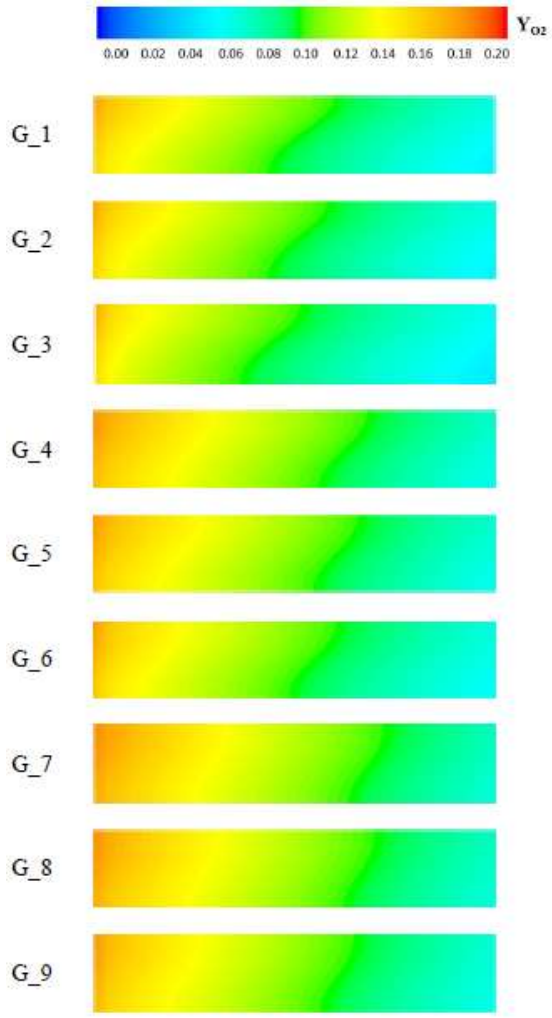

Fig. 8. Contour of oxygen mole fraction at GDL/CL interface for constant oxygen utilization and V= 0.35 V

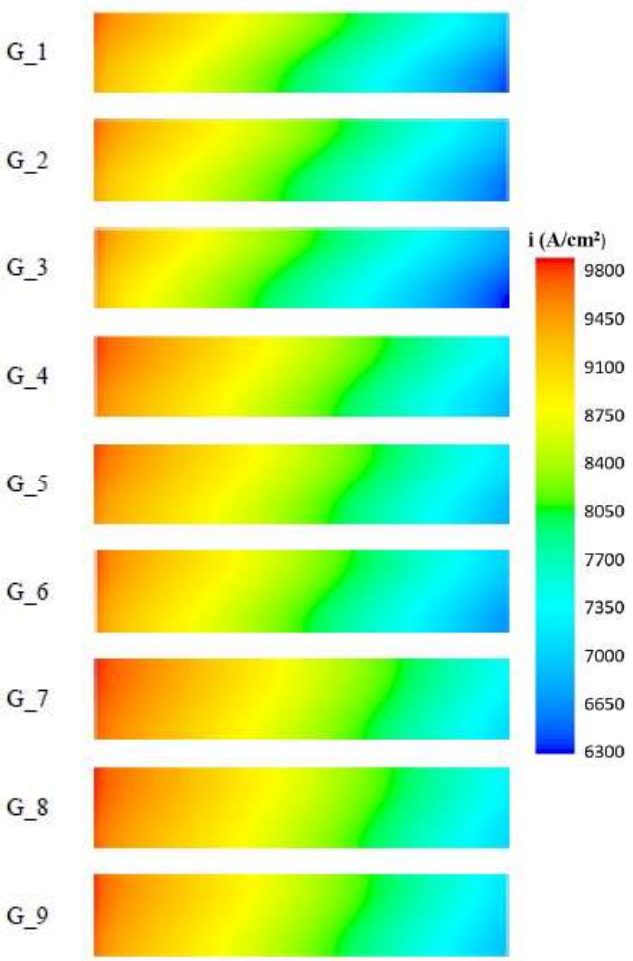

Fig. 9. Contour of current density at GDL/CL interface for constant oxygen utilization and V= 0.35 V

is noted that, the mass flow through the channels is the primary parameter affecting the pressure drop. In each computed case, the mass flow is fixed by the 50% utilization and the given V_{cell}. According to the polarization curve, smaller V_{cell} values correspond to larger i, larger $\dot{m}$, and larger $\Delta P_{in\rightarrow out}$. Column 10 represents the pressure gradient along the channel. This parameter demonstrates the ability of working fluid to purge the water condense towards the channel outlet and also prevents flooding [20, 21]. Column 12 represents the pumping power, which is required to drive the working fluid through the channel. It is determined from $P_{Pump} = \Delta P \dot{V} / A$,where $\dot{V}$ is the average volume flow rate in channel, and A is the cell active area. Column 13 represents the generated cell power density, $P_g = i.V_{cell}$. And the last column is the net cell power density which calculated from equation (1). Fig. 10 depicts pressure gradient amount for all cases (G_1 to G_9) in mbar/m and proportional to cell voltage 0.2, 0.35, 0.5 and 0.65 V and constant oxygen utilization. Small pressure gradient results in remaining liquid water inside the channel and in turn decreases the efficiency of the cell. So surveying amount of pressure drop alongside the channel is recommended. Lower limit considered for all the calculation domain is 20 mbar/m. Large pressure gradient results in pumping power increment and non-uniform distribution of pressure in MEA. So upper limit considered for the whole calculation domain is 200 mbar/m [21-24]. Cases with pressure gradient

Table 3 Summary of the results for constant oxygen utilization

[1]Case	[2]w/2 mm	[3]d/2 mm	[4]h mm	[5] $\dot{m}\times10^7$ (kg/s)	[6]i (A/cm^2)	[7]V_{cell} (V)	[8]u	[9] $\Delta P_{in\to out}$ (Pa)	[10] $\frac{\Delta P_{in\to out}}{L}$ (mbar/m)	[11]$Y_{O2@GDL/CL}$	[12]PPump (W/cm^2)	[13]Pg (W/cm^2)	[14]Pnet (W/cm^2)
G_1	0.25	0.5	0.4	8.52	1.9025	0.2	0.5	1550.49	193.81	0.08095	0.00214	0.38050	0.37836
				4.25	0.9492	0.35	0.5	911.83	113.98	0.10430	0.00063	0.33222	0.33159
				1.22	0.2715	0.5	0.5	283.29	35.41	0.12396	0.00006	0.13575	0.13569
				0.14	0.0302	0.65	0.5	355.68	44.46	0.12234	0.00001	0.01963	0.01962
G_2	0.25	0.5	0.6	8.28	1.8494	0.2	0.5	695.48	86.94	0.07215	0.00094	0.36988	0.36895
				4.24	0.9476	0.35	0.5	350.95	43.87	0.10334	0.00024	0.33166	0.33142
				1.22	0.2734	0.5	0.5	116.04	14.50	0.12504	0.00002	0.13670	0.13668
				0.14	0.0323	0.65	0.5	35.40	4.43	0.13215	0.00000	0.02100	0.02099
G_3	0.25	0.5	0.8	8.00	1.7868	0.2	0.5	425.22	53.15	0.06414	0.00055	0.35736	0.35681
				4.15	0.927	0.35	0.5	218.58	27.32	0.09738	0.00015	0.32445	0.32430
				1.21	0.2692	0.5	0.5	71.58	8.95	0.12230	0.00001	0.13460	0.13459
				0.14	0.0318	0.65	0.5	35.21	4.40	0.12971	0.00000	0.02067	0.02067
G_4	0.35	0.4	0.4	8.83	1.9702	0.2	0.5	917.05	114.63	0.09393	0.00131	0.39404	0.39273
				4.39	0.9812	0.35	0.5	408.45	51.06	0.11433	0.00029	0.34342	0.34313
				1.24	0.277	0.5	0.5	86.36	10.79	0.12838	0.00002	0.13850	0.13848
				0.14	0.0306	0.65	0.5	206.85	25.86	0.12434	0.00000	0.01989	0.01989
G_5	0.35	0.4	0.6	8.67	1.935	0.2	0.5	372.09	46.51	0.08683	0.00052	0.38700	0.38648
				4.37	0.9765	0.35	0.5	166.01	20.75	0.11240	0.00012	0.34178	0.34166
				1.24	0.2768	0.5	0.5	62.86	7.86	0.12782	0.00001	0.13840	0.13839
				0.15	0.0325	0.65	0.5	12.21	1.53	0.13284	0.00000	0.02113	0.02112
G_6	0.35	0.4	0.8	8.48	1.894	0.2	0.5	200.10	25.01	0.08052	0.00028	0.37880	0.37852
				4.30	0.9605	0.35	0.5	106.45	13.31	0.10732	0.00007	0.33618	0.33610
				1.23	0.2738	0.5	0.5	34.20	4.27	0.12573	0.00001	0.13690	0.13689
				0.14	0.032	0.65	0.5	15.89	1.99	0.13046	0.00000	0.02080	0.02080
G_7	0.45	0.3	0.4	8.97	2.0033	0.2	0.5	667.09	83.39	0.10245	0.00097	0.40066	0.39969
				4.47	0.9975	0.35	0.5	330.97	41.37	0.11957	0.00024	0.34913	0.34889
				1.25	0.2794	0.5	0.5	152.59	19.07	0.12964	0.00003	0.13970	0.13967
				0.14	0.0313	0.65	0.5	143.81	17.98	0.12746	0.00000	0.02035	0.02034
G_8	0.45	0.3	0.6	8.91	1.9886	0.2	0.5	235.59	29.45	0.09878	0.00034	0.39772	0.39738
				4.45	0.9931	0.35	0.5	114.61	14.33	0.11794	0.00008	0.34759	0.34750
				1.25	0.2799	0.5	0.5	32.30	4.04	0.13019	0.00001	0.13995	0.13994
				0.15	0.0329	0.65	0.5	5.24	0.66	0.13497	0.00000	0.02139	0.02138
G_9	0.45	0.3	0.8	8.76	1.9566	0.2	0.5	128.41	16.05	0.09219	0.00018	0.39132	0.39114
				4.39	0.9794	0.35	0.5	64.87	8.11	0.11335	0.00005	0.34279	0.34274
				1.24	0.277	0.5	0.5	20.17	2.52	0.12812	0.00000	0.13850	0.13850
				0.14	0.0322	0.65	0.5	6.67	0.83	0.13197	0.00000	0.02093	0.02093

1 Geometry name; 2Channel width; 3Rib size; 4Channel height; 5The supplied mass flow rate; 6Cell current density; 7Cell voltage; 8Utilization factor; 9Pressure drop from inlet to the exit of the channel; 10Pressure gradient along the channel; 11Oxygen mole fraction at the GDL/CL interface; 12Pumping power to drive the working fluid along the channel; 13The generated cell power; 14The net generated electrical power from the cell (see Eqn. (1) for detail).

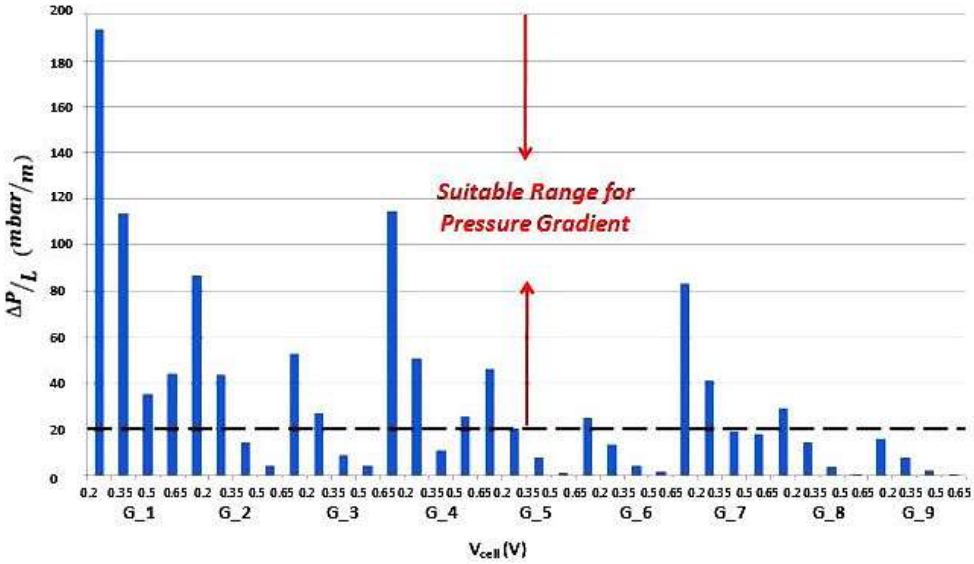

Fig. 10. Pressure gradient amount for all cases in mbar/m and proportional to cell voltage 0.2, 0.35, 0.5 and 0.65 V and constant utilization

drawn between two parallel lines are considered as desired cases. Following graphs show the first step of data reduction.

Fig. 11 shows the variation of net power density with oxygen mole fraction at the face of GDL/CL interface at operating voltages 0.2 to 0.65 V, for cases G_1 to G_9. As shown in this figure, this variation is linear and the equations are as follows:

$$P_{net} = 1.114 Y_{O_2} + 0.287 \quad (16)$$

$$P_{net} = 1.118 Y_{O_2} + 0.215 \quad (17)$$

$$P_{net} = 0.672 Y_{O_2} + 0.052 \quad (18)$$

$$P_{net} = 0.140 Y_{O_2} + 0.002 \quad (19)$$

Generally, equations 16 to 19 can be written:

$$P_{net} = a Y_{O_2} + b \quad (20)$$

For any channel geometry, in a specific operating voltage and a simple and fast numerical simulation with fixed sink and source in CL, using the charts given in fig. 12 and equation 20, the cell net power density would be achieved. The procedure is described in fig. 13.

6. Concluding Remarks

• The oxygen mole fraction (YO_2) that represents the content of oxygen at the face of reaction site (GDL/CL interface), at regions above the channel is more than the regions above the ribs. The content of oxygen increases by increasing the channel width and decreases by increasing the rib width.

• The oxygen mole fraction is directly proportional to the produced current density. The cases with larger channel width have richer oxygen contents within the CL, hence, they produce more electrical current.

• For all of the cases considered, it is observed that for a given cell voltage, the net power density of the cell linearly varies with oxygen mole fraction $(YO_2)_{CL}$ (see Figs. 11(a) to 11(d)).

•Using the methods of data reduction in this paper, it has become possible to predict how much enhancement in electrical power can be achieved due to 1% enrichment in oxygen content within the CL. For instance, it is observed that at V=0.35 V, for 1% enrichment in oxygen content within the CL, 3.5% net power enhancement can be achieved.

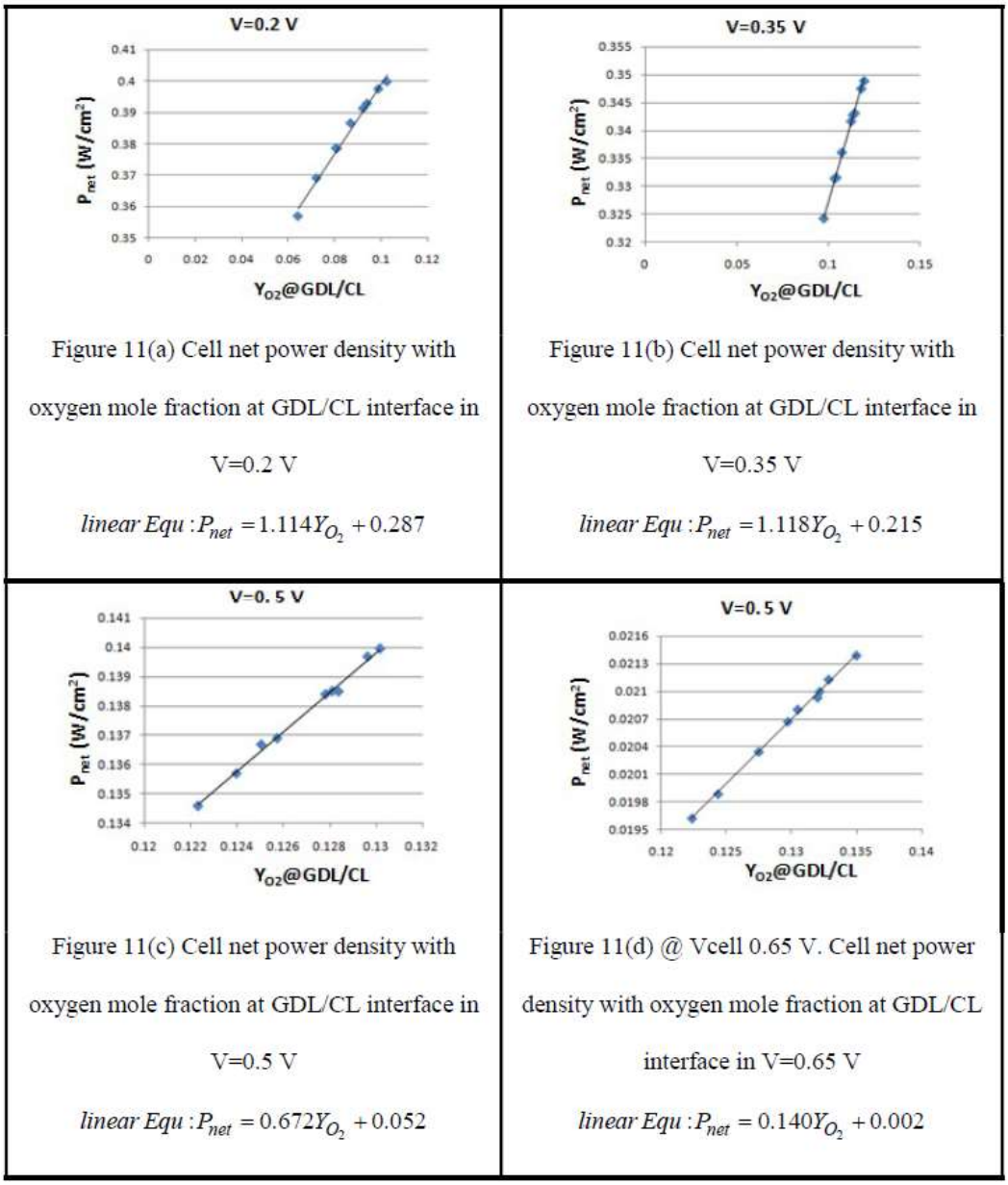

Figure 11(a) Cell net power density with oxygen mole fraction at GDL/CL interface in V=0.2 V

$linear\ Equ: P_{net} = 1.114 Y_{O_2} + 0.287$

Figure 11(b) Cell net power density with oxygen mole fraction at GDL/CL interface in V=0.35 V

$linear\ Equ: P_{net} = 1.118 Y_{O_2} + 0.215$

Figure 11(c) Cell net power density with oxygen mole fraction at GDL/CL interface in V=0.5 V

$linear\ Equ: P_{net} = 0.672 Y_{O_2} + 0.052$

Figure 11(d) @ Vcell 0.65 V. Cell net power density with oxygen mole fraction at GDL/CL interface in V=0.65 V

$linear\ Equ: P_{net} = 0.140 Y_{O_2} + 0.002$

Fig. 11. Cell net power density with oxygen mole fraction at GDL/CL interface

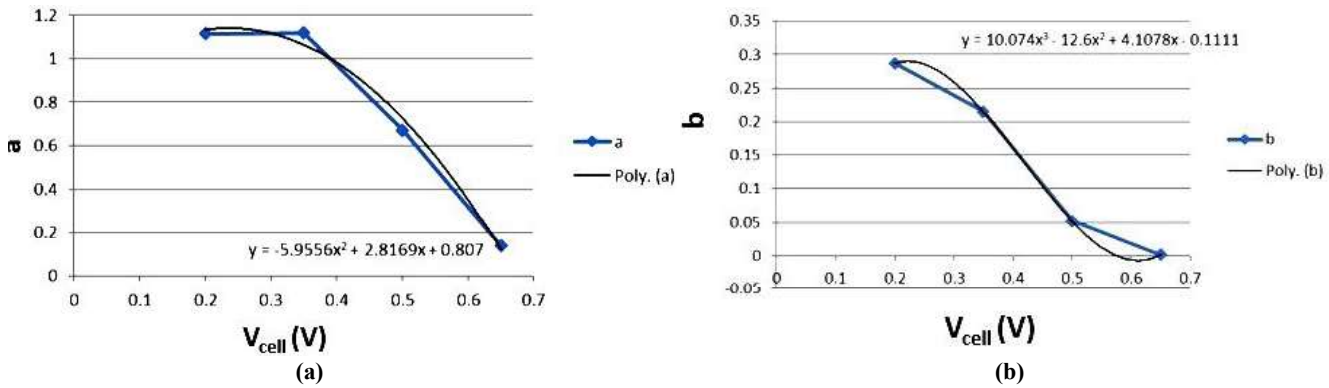

Fig. 12. Variation of parameters a and b in equation 15 with operating voltage

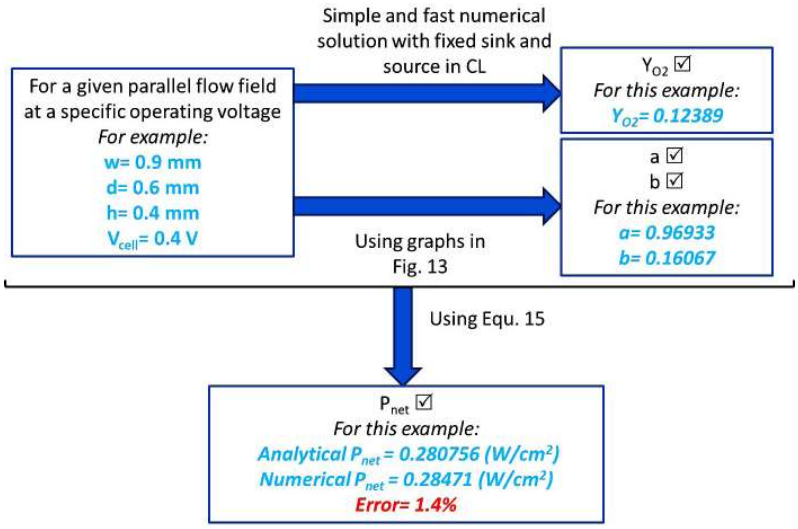

Fig. 13. Procedure of calculating analytical net power density

Acknowledgement

Financial supports for this project are provided from Alexander von Humboldt Foundation, Germany and Amirkabir University of Technology, Iran. Thanks to Ulm University for paving the usage of the academic version of ANSYS® FLUENT®.

References

[1] X. Wang, Y. Duan, W. Yan, X. Peng, Local Transport Phenomena and Cell Performance of PEM Fuel Cells with Various Serpentine Flow Field Designs, J. Power Sources, 175(2008) 397-407.

[2] P. Ramesh, S.P. Duttagupta, Effect of Channel Dimensions on Micro PEM Fuel Cell Performance Using 3D Modeling, Int. J. Renewable Energy Res, 3(2)(2013) 353-358.

[3] H.R. Choghadi, M.J. Kermani, 15% Efficiency Enhancement Using Novel Partially Interdigitated Serpentine Flow Field for PEM Fuel Cells, 10th International Conference on Sustainable Energy Technologies SET2011, Istanbul, Turkey, 2011.

[4] D.M. Bernardi, M.W. Verbrugge, A Mathematical Model of the Solid-Polymer-Electrolyte Fuel Cell, J. Electrochem., 139(9)(1992) 2477-2491.

[5] M. Khakbaz-Baboli, M.J. Kermani, A Two-Dimensional, Transient, Compressible Isothermal and Two-Phase Model for the Air Side Electrode of PEM Fuel Cell, J. Electrochemical Acta, 53(2008) 7644-7654.

[6] O. Okada, K. Yokoyama, Development of Polymer Electrolyte Fuel Cell Cogeneration Systems for Residential Applications, Fuel Cells- From Fundamentals to Systems, 1(1)(2001).

[7] M. Thoennes, A. Busse, L. Eckstein, Forecast of Performance Parameters of Automotive Fuel Cell Systems – Delphi Study Results, Fuel Cells- From Fundamentals to Systems, 14(6)(2014) 781- 791.

[8] C. Wieser, Novel Polymer Electrolyte Membrane for Automotive Applications Requirements and Benefits, Fuel Cells- From Fundamentals to Systems, 4(4)(2004) 245- 250.

[9] P. Britz, N. Zartenar, PEM Fuel Cell Systems for Residential Applications, Fuel Cells- From Fundamentals to Systems, 4(4)(2004) 269- 275.

[10] B.K. Kakati, V. Mohan, Development of Low-Cost Advanced Composite Bipolar Plate for Proton Exchange Membrane Fuel Cell, Fuel Cells- From Fundamentals to Systems, 8(1)(2008) 45- 51.

[11] O. Shamarina, A.A.Kulikovsky, A.V. Chertovich,

A.R. Khokhlov, A Model for High-Temperature PEM Fuel Cell The Role of Transport in the Cathode Catalyst Layer, Fuel Cells- From Fundamentals to Systems, 12(4) (2012) 577- 582.

[12] P.Y. Yi, L.F. Peng, X.M. Lai, D.A. Liu, J. Ni, A Novel Design of Wave-Like PEMFC Stack with Undulate MEAs and Perforated Bipolar Plates, Fuel Cells- From Fundamentals to Systems, 10(1)(2010) 111- 117.

[13] K.S. Choi, B.G. Kim, K. Park, H.M. Kim, Current Advances in Polymer Electrolyte Fuel Cells Based on the Promotional Role of Under-rib Convection, Fuel Cells- From Fundamentals to Systems, 12(6)(2012) 908- 938.

[14] D. Tehlar, R. Fluckiger, A. Wokaun, F.N. Buchi, Investigation of Channel-to-Channel Cross Convection in Serpentine Flow Fields, Fuel Cells- From Fundamentals to Systems, 10(6)(2010) 1040- 1049.

[15] J. Wang, H. Wang, Flow-Field Designs of Bipolar Plates in PEM Fuel Cells Theory and Applications, Fuel Cells- From Fundamentals to Systems, 12(6)(2012) 989-1003.

[16] H.C. Liu, W.M. Yan, C.Y. Soong, F. Chen, H.S. Chu, Reactant Gas Transport and Cell Performance of Proton Exchange Membrane Fuel Cells with Tapered Flow Field Design, J. Power Sources 158 (2006) 78-87.

[17] P. Ramesh, S.P. Duttagupta, Effect of Channel Dimensions on Micro PEM Fuel Cell Performance Using 3D Modeling, Int. J. renewable energy research, 3(2) (2013).

[18] M.J. Kermani, J.Scholta, Influences of a More Satisfactory Catalyst Layer Boundary Conditions in the Design of PEM Fuel Cell Flow Fields, 14th Ulm Electrochemical Talks, Ulm, Germany, 2014.

[19] A. Ghanbarian, M.J. Kermani, J. Scholta, M. Abdollahzadeh, Polymer Electrolyte Membrane Fuel Cell Flow Field Design Criteria- Application to Parallel Serpentine Flow Patterns, Energy conversion and management, 166(2018)281-296.

[20] S. Hasmady, M.P. Wacker, K. Fushinobu, K. Okazaki, Treatment of Heterogeneous Electro Catalysis in Modeling Transport Reaction Phenomena in PEFCS, ASME-JSME Thermal Engineering Summer Heat Transfer Conference, Vancouver, British Columbia, Canada, 2007.

[21] N. Akhtar, A. Qureshi, J. Scholta, Ch. Hartnig, M. Messerschmidt, W. Lehnert, Investigation of Water Droplet Kinetics and Optimization of Channel Geometry for PEM Fuel Cell Cathodes, Int. J. Hydrogen Energy 34 (2009) 3104 – 3111.

[22] M. Klages, S. Enz, H. Markötter, I. Manke, N. Kardjilov, J. Scholta, Investigations on Dynamic Water Transport Characteristics in Flow Field Channels Using Neutron Imaging Techniques, J. Power Sources 239 (2013) 596-603.

[23] A. Ghanbarian, M.J. Kermani, Performance Improvement of PEM Fuel Cells Using Air Channel Indentation; Part I: Mechanisms to Enrich Oxygen Concentration in Catalyst Layer, Iranian J. Hydrogen and Fuel Cell, 3(2014) 199-207.

[24] A. Ghanbarian, M.J. Kermani, Enhancement of PEM Fuel Cell Performance by Flow Channel Indentation, Energy Conversion and management, 110 (2016) 356–366.